QUARTERLY JOURNAL OF THE ROYAL METEOROLOGICAL SOCIETY
RMetS Royal Meteorological Society

Non-local convergence coupling in a simple stochastic convection model

Journal:	*QJRMS*
Manuscript ID:	Draft
Wiley - Manuscript type:	Research Article
Date Submitted by the Author:	n/a
Complete List of Authors:	Brenowitz, Noah; Courant Institute of Mathematical Science, Mathematics Frenkel, Yevgeniy; Courant Institute of Mathematical Sciences, New York University, Mathematics Majda, Andrew; Courant Institute of Mathematical Sciences, New York University, Mathematics
Keywords:	Stochastic convective parameterisation, wave-CISK, tropical atmospheric dynamics, convectively coupled waves

Non-local convergence coupling in a simple stochastic convection model

Noah D. Brenowitz*, Yevgeniy Frenkel, Andrew J. Majda

Department of Mathematics and Center for Atmosphere Ocean Science, Courant Institute of Mathematical Sciences, New York University, New York, NY, USA

*Correspondence to: N. D. Brenowitz, Department of Mathematics and Center for Atmosphere Ocean Science, Courant Institute of Mathematical Sciences, New York University, 251 Mercer St., New York, NY 10012, USA. Email: noah@cims.nyu.edu.

Recent observational studies show a strong link between large-scale wind convergence, precipitation and convective cloud fraction. However, using this as a physical assumption in a model typically leads to deleterious wave-CISK behaviour such as grid-scale noise. The quasi-equilibrium (QE) schemes ameliorate these issues, but still inadequately represent convection. This controversy is revisited here in the context of a simple stochastic one baroclinic mode theoretical model which mimics aspects of operational QE parameterisations. A version of this model is implemented which couples the stochastic formation of convection to the wind convergence. Linearised analysis shows that using the *local* convergence results in a classic wave-CISK standing instability where the growth rate increases with the wavenumber. However, using a large-scale averaged convergence restricts the instability to physically plausible scales and provides a physically-motivated mechanism for non-local interactions in a simple convection scheme. In nonlinear stochastic simulations with a non-uniform imposed sea surface temperature (SST) field, the non-local convergence coupling introduces desirable intermittent variability on intraseasonal time scales. Moreover, the convergence coupling leads to a circulation with a similar mean but higher variability than the equivalent parameterisation without convergence coupling. Finally, the model is shown to retain these features on fine and coarse mesh sizes.

Key Words: Stochastic convective parameterisation, wave-CISK, tropical atmospheric dynamics, convectively coupled waves

Received . . .

1. Introduction

The realistic representation of cumulus convection in coarse resolution models is a central problem in tropical meteorology, climate modelling, and numerical weather prediction. These flows are characterised by the cooperation of multiple spatial and temporal scales from mesoscale convective systems to synoptic scale convectively coupled waves to the planetary scale Madden Julian Oscillation (Nakazawa 1988; Kiladis *et al.* 2009; Lau and Waliser 2012). The multiscale nature of the problem remains a key obstacle to the development of accurate convective parameterisations, and the current generation of coarse resolution General Circulation Models (GCMs) still poorly represents dynamics in tropical regions (Slingo *et al.* 1996; Moncrieff and Klinker 1997; Scinocca and McFarlane 2004; Lau and Waliser 2012; Zhang 2005). That said, there have been some recent improvements in a few GCMs (Khouider *et al.* 2011; Del Genio *et al.* 2012; Crueger *et al.* 2013; Deng *et al.* 2015; Ajayamohan *et al.* 2013, 2014).

Conventional cumulus parameterisations are typically based on the quasi-equilibrium (QE) assumption (Arakawa and Schubert 1974; Zhang and McFarlane 1995; Emanuel *et al.* 1994), the moist convective adjustment idea (MANABE *et al.* 1965), or a large-scale moisture convergence closure (Kuo 1974; Tiedtke 1989). In all of these, the mean response of unresolved modes on resolved variables is formulated according to various prescribed deterministic closures (Kain and Fritsch 1990; Betts and Miller 1986; Zhang and McFarlane 1995). Of particular relevance to modern parameterisation, the QE hypothesis assumes that the ensemble of clouds within a particular grid box approximately balances the creation of conditional instability by large-scale processes. The QE hypothesis has proved especially useful for coarse resolutions, and it underpins many operational convection schemes (Betts and Miller 1986; Zhang and McFarlane 1995; Arakawa 2004). See Raymond and Herman (2011) for a more contemporary perspective on QE.

These convective schemes are accompanied by distinct theories for the large-scale instability and organisation of tropical flows. The moisture convergence closures are closely related to the theory of Convective Instability of the Second Kind (CISK) (Charney and Eliassen 1964). CISK is based on the idea that small-scale convection cooperates to induce boundary-layer convergence on large scales, which then supplies moisture for additional convection. While the original theory was developed for the purposes of tropical cyclones, wave-CISK is an alternate theory which is relevant in the absence of rotation (Lindzen 1974). Unfortunately, wave-CISK predicts a small-scale standing instability with growth rates that increase with wave-number, which is a highly unrealistic result. In simulations using a moisture convergence closure, this can manifest as grid-scale precipitation.

As a whole, the moisture convergence closures and CISK have been criticised in favour of QE-based schemes and a QE-compatible instability mechanism known as wind induced surface heat exchange (WISHE) (Emanuel *et al.* 1994). WISHE is a mechanism where ocean surface sensible and latent heat fluxes depend on the magnitude of the surface winds. This non-linearity drives a positive feedback loop between evaporation, deep convection, and wind convergence due to convective updraughts. On the other hand, the CISK hypothesis states that convergence in the boundary layer directly results in convective heating of the atmosphere regardless of ocean surface fluxes. Both WISHE and CISK were originally introduced as mechanisms for the development and intensification of tropical cyclones; however, their importance for organised convection is debatable (Grabowski *et al.* 2000).

In spite of these concerns, there is substantial observational evidence highlighting the strong link between convection and moisture convergence. Comparing radar data from Darwin, Australia to large-scale fields from a reanalysis product indicates that convection better correlates with large-scale vertical velocity at 500 hPa than it does with humidity or convectively available potential energy (CAPE) (Davies *et al.* 2013). These data also show that a stochastic multicloud model has more realistic statistics when using vertical velocity versus CAPE as a predictor for convection (Peters *et al.* 2013)—a conclusion which is shared by a systematic study of trigger functions in operational convective schemes (Suhas and Zhang 2014). However, because these studies are performed diagnostically using data from a single location, they cannot make statements of causality or address the dynamical criticisms of Emanuel *et al.* (1994).

These criticisms, however, do not take into account the advances in convective parameterisations of the last decade. One of these improvements has come from relaxing the QE assumption through the addition of a stochastic perturbation (Buizza *et al.* 1999; Lin 2003; Majda and Khouider 2002; Khouider *et al.* 2003; Majda *et al.* 2008; Majda and Stechmann 2008). Of these, a simple and promising approach has been the use of Markov-chain lattice models to represent unresolved sub-grid variability (Majda and Khouider 2002; Khouider *et al.* 2003, 2010; Crommelin and Vanden-Eijnden 2008). The simplified stochastic model for convective inhibition (CIN) introduced in Majda and Khouider (2002); Khouider *et al.* (2003) (hereafter MK02 and KMK03) is of particular relevance here. In that work, a coarse-resolution 1-1/2 layer model that mimics aspects of QE-based GCM convective schemes was coupled to a stochastic lattice model within each coarse-grid cell. For a clear description and linearised analysis of the corresponding deterministic model, the reader should refer to Majda and Shefter (2001b) (hereafter MS01). Each element of this lattice is either convectively active or in a state of convective inhibition (CIN). The lattice elements, which are called CIN sites, are allowed to interact with each other and with the large-scale environment through the boundary-layer equivalent potential temperature. This stochastic process, which is known as a continuous time Markov chain, is closely related to the Ising spin-flip models used to study phase-transitions in material science (Majda and Khouider 2002; Katsoulakis *et al.* 2003b). While the lattice dynamics can be computationally expensive, there is a suitable cheap coarse-graining which produces a stochastic process for the cloud area fractions in each coarse grid cell (Katsoulakis *et al.* 2003a; Khouider *et al.* 2003). These stochastic dynamics are not amenable to theoretical analysis, but, as the number of lattice elements increases, the dynamics approach a deterministic limit known as the mean-field limit equations (DMFLEs). Therefore, the stochastic scheme can be studied in a similar fashion as MS01 by performing linearised analysis of the DFMLEs.

As suggested in Palmer (2001), successful stochastic parameterisations should be non-local in nature. In the context of convective parameterisation, this essentially means that the stochastic process for the cloud fractions in a particular grid-box should depend on other grid boxes. The triggering of convection by large-scale wind-convergence, viewed in this light, is a fundamentally non-local interaction (Peters *et al.* 2013). Therefore, coupling a coarse-resolution stochastic model to the large-scale convergence field could yield substantial improvements over related deterministic parameterisations.

In this paper, we extend the work of Peters *et al.* (2013) to a fully prognostic and spatially extended convection model using the stochastic modelling tools described above. The aim here is to develop a prototype stochastic convection parameterisation that takes into account the effects of large-scale convergence and avoids the pitfalls of moisture convergence closures and wave-CISK. For the sake of simplicity, this study is carried out using the stochastic CIN model described in KMK03. As described above, this model lacks the second baroclinic structure necessary for the realistic representation of organised convection, and is designed to mimic aspects of traditional QE-based GCMs. This allows us to unambiguously study the dynamical consequences of convergence coupling and to suggest a path towards improving standard operational schemes.

In detail, a version of the stochastic CIN parameterisation with non-local convergence coupling is studied. As in MS01 and KMK03, the parameterisation is coupled to a vertical truncation of the primitive equations. Emphasis is placed on elucidating the role of non-local interactions and differentiating the model from typical wave-CISK behaviour. Linear analysis of the DMFLEs shows that the *local* version of the model has small-scale instability associated with wave-CISK. On the other hand, the scale-selective bands of instability with diminishing growth rates introduced by *non-local* convergence coupling can be associated with the multiscale nature of convection. Spatially extended simulations confirm the predictions of this linear theory and reveal low-frequency variability on a time scale associated with the convergence coupling. This low-frequency variability manifests as intermittent convectively coupled waves (CCWs) that are similar to those observed in CRM and high resolution GCMs, even though the model here only has one mode of vertical resolution. A key finding here is that a stochastic parameterisation with non-local convergence coupling can be thought of as a powerful surrogate

for unresolved horizontal and vertical convective organisation, as argued by Peters *et al.* (2013).

The remainder of the paper is organised as follows. A self-contained review of the stochastic CIN parameterisation is presented in Section 2. Emphasis is placed on the connection with deterministic mass flux parameterisations and the introduction of the non-local stochastic convergence coupling. In Section 3, linear analysis of the DMFLEs is used to compare the effects of local and non-local convergence coupling. The sensitivity to the key parameters is also studied. In Section 4, the modified parameterisation is used to generate flows above the equator on grids of varying resolution (40–160 km) in a series of idealised Walker cell simulations. Some discussion and concluding remarks are given in Section 5.

2. Model formulation

The stochastic model in this paper is an extension of a deterministic model which was analysed in MS01. The model only has one vertical heating mode, which can be interpreted as a mass flux, and is a simplified version of QE-based mass-flux schemes like that of (Zhang and McFarlane 1995) which is amenable to theoretical analysis.

The vertical structure is determined by projection of primitive equations on a first baroclinic heating mode (Majda and Shefter 2001b,a). The prognostic variables are the zonal component of the fluid velocity, the tropospheric potential temperature, and the equivalent potential temperatures in the boundary layer and the mid-troposphere. The non-dimensional dynamic equations for these in variables are given by

$$\frac{\partial u}{\partial t} - \frac{\partial \theta}{\partial x} = -\frac{1}{\tau_D} u \tag{1}$$

$$\frac{\partial \theta}{dt} - \frac{\partial \theta}{\partial x} = Q_c - Q_R^0 - \frac{1}{\tau_R}\theta \tag{2}$$

$$h_b \frac{\partial \theta_{eb}}{\partial t} = -D(\theta_{eb} - \theta_{em}) + E \tag{3}$$

$$H \frac{\partial \theta_{em}}{\partial t} = D(\theta_{eb} - \theta_{em}) - H\left(Q_R^0 + \frac{1}{\tau_R}\theta\right). \tag{4}$$

The typical dimensional scales of these variables is contained in Table 1. The u and θ equations together comprise a singled force shallow water equation, which is forced by radiation, $Q_R^0 + \tau_R^{-1}\theta$, convective heating, Q_c, and velocity drag, $\tau_D^{-1}u$. The convective heating, $Q_c = \sigma_c w_c$ is the product of the convective area fraction and convective mass flux. The mass flux for convective regions is approximated by $w_c = \sqrt{R_c \cdot CAPE^+}$, where $CAPE = \theta_{\text{eb}} - \gamma\theta$, and R_c is a fixed constant (Majda and Shefter 2001b, see eq. (2.13)).

The equations for the moist variables θ_{eb} and θ_{em} are forced by evaporation, radiation, and downdraughts. The constants h_b and H respectively denote the depth of the boundary layer and the typical height of penetrative clouds. The mass-flux due to downdraughts is given by the sum of the net environmental subsidence and convective downdraughts,

$$\frac{D}{h_m} = (Q_c + u_x)^+ + \frac{1-\mu}{\mu} Q_c,$$

where $0 \leq \mu \leq 1$ is the precipitation efficiency (Majda and Shefter 2001a; MS01). The mid-tropospheric height, h_m, is used because downdraughts only exchange mass between the lower troposphere and the boundary layer. The evaporation is modelled as a wind-dependent drag-law with the form given by

$$\frac{E}{h_b} = \left(\tau_e^{-1} + \frac{C_\theta}{h_b}|u|\right)(\theta_{eb}^\star - \theta_{eb}). \tag{5}$$

This evaporation depends on the magnitude of the velocity and therefore gives rise to WISHE. The velocity associated with a convectively coupled wave (CCW) increases the evaporation of moisture from the boundary layer and has a positive feedback effect on convection. Moreover, in the presence of a mean wind field, WISHE leads to propagating unstable disturbances. Since this behaviour has been explored in MS01, we will disable WISHE in the linear analysis of Section 3 by setting $C_\theta = 0$. In this case, evaporation occurs with a fixed time scale of $\tau_e =$ 8 hrs. While there is scant observational evidence that WISHE drives large-scale CCWs (Lin and Neelin (2000); Holloway and Neelin (2009) and references therein), it is commonly used to generate instabilities in deterministic GCM parameterisations that otherwise lack variability. Likewise, WISHE is used in the nonlinear simulations of Section 4.

Having described all of the deterministic closures, it remains to describe how the convective area fraction σ_c is given by a

stochastic process, and, specifically, how non-local convergence coupling enters this formulation.

2.1. *Stochastic CIN model*

Here, we briefly review the stochastic model for convective inhibition (CIN) introduced in Majda and Khouider (2002). CIN can be thought of as a barrier for deep penetrative convection in the tropics, and it is known to have important fluctuations on the order of 1 km, which is much smaller than typical GCM resolution. Changes in CIN can be attributed to a multitude of different mechanisms in the turbulent boundary layer, such as gust fronts, gravity waves, turbulent fluctuations in equivalent potential temperature, and surface heat fluxes (Mapes 2000, and references therein). To model CIN, Majda and Khouider used an Ising lattice model, where each coarse grid cell is subdivided into a microscopic lattice grid. The lattice elements, which we also refer to as CIN sites, interact with each other and with the coarse-grid deterministic flow variables according to the following rules:

1. If a CIN site is surrounded by mostly CIN sites it has higher probability to remain a CIN site.
2. If a non-CIN site is surrounded by mostly CIN sites it has higher probability to switch to a CIN site.
3. The coarse grid-cell values supply an external potential which either promotes CIN or active convection according to reasonable physical assumptions.

Evolving the full microscopic lattice system is computationally expensive, so in KMK03, the authors start with the microscopic dynamics, and derive a coarse-grained birth-death process for the total fraction of CIN within a coarse-grid cell. A systematic approach to coarse-graining such processes has been developed in Katsoulakis *et al.* (2003b,a). Here, we briefly describe the birth-death process that was derived in KMK03. In that work, the stochastic dynamics are coupled to the boundary layer temperature θ_{eb} through the external potential (c.f. item 3 above). The main modification in the current study is to extend this potential to include dependence on the large-scale averaged wind convergence field.

For each cell of the numerical PDE discretisation $\triangle x_k,\ k = 1, .., m$, the CIN fraction, $\sigma_k(t)$, can be treated as a birth-death process, which takes values from 0 to 1 with increments of $\triangle\sigma = 1/q$, where q is the number of elements in the underlying microscopic lattice. The convective cloud fraction can be obtained by a simple relation $\sigma_c = (1-\sigma)\sigma_c^+$, where σ_c^+ is a maximum convective cloud fraction, $\sigma_c^+ = .01$. The birth-death process evolves according to the following transition rates

$$Prob\{\sigma_k(t+\triangle t) = \sigma_k(t) - \triangle\sigma\} = C_d(t)\triangle t + O(\triangle t), \quad (6)$$

$$Prob\{\sigma_k(t+\triangle t) = \sigma_k(t) + \triangle\sigma\} = C_a(t)\triangle t + O(\triangle t). \quad (7)$$

The birth-death rates are given by

$$C_a(\sigma_k) = \frac{1}{\tau_q}(1-\sigma_k), \quad (8)$$

$$C_d(\sigma_k) = \frac{1}{\tau_q}\sigma_k e^{-V(\sigma_k)}, \quad (9)$$

where $\tau_q = \tau_I/q$ is the time scale associate with the transitions of the sum of the micro-lattice sites. Here V is a coarse-grained Hamiltonian function that includes contributions from the interactions between microscopic CIN sites and an external potential which depends on the large scale dynamics. It is given by the form

$$V(\sigma_k) = 2\beta\frac{q\sigma_k - 1}{q-1} + h_{ext}, \quad (10)$$

where h_{ext} is the external potential. The term proportional to the constant β comes from averaging the self-interactions of the microscopic CIN elements within the coarse cell and acts as an energy barrier. The formulation of rates above comes from the Arrhenius-like dynamics potential of the microscopic model (Majda and Khouider 2002).

For the purposes of the linear analysis below, it is necessary to use a deterministic limit of these stochastic dynamics. Subtracting (6) from (7), normalising by $\triangle t$, and taking the limit as q goes to infinity gives a small fluctuation deterministic limit of the stochastic process. The resulting system is known as the deterministic mean field limit equations (DMFLEs) (Katsoulakis *et al.* 2003b,a; MK02; KMK03), and is comprised of (1)–(4) along with a deterministic equation for the cloud fraction which is given by

$$\frac{\partial\sigma_k}{\partial t} = \frac{1}{\tau_q}(1-\sigma_k) - \frac{1}{\tau_q}\sigma_k\exp(-2\beta\sigma_k - h_{ext}). \quad (11)$$

Parameter	Value	Description
T	8.33 hr	Equatorial time scale
L	1500 km	Equatorial Rossby radius
Θ	15 K	Temperature fluctuation scale
c	50 m s^{-1}	Velocity scale
h_b	500 m	Boundary layer depth
h_m	5 km	Middle tropospheric height
H	8 Km	Average depth of convective cloud
Q_R^0	1 K day^{-1}	First baroclinic radiative cooling rate
θ_0	300 K	Reference temperature
$\theta_{eb}^\star$	380 K	Saturation equivalent potential temp. in boundary layer
σ_c^+	.01	Maximum convective area fraction
c_p	1.00 kJ K kg^{-1}	Specific heat capacity of dry air
Γ_m	6 K km^{-1}	Moist lapse rate
γ	1.6	Ratio of dry and moist lapse rates
R_c	$2Hc_p\Gamma_m(h_m g)^{-1}$ s^{-2}	CAPE coefficient
τ_D	2.8 days	Momentum relaxation time scale
τ_R	50 day	Newtonian cooling time scale
τ_e	8 hours	Surface evaporation time scale
C_θ	$1.3 \cdot 10^{-3}$	WISHE coefficient
q	12	Number of stochastic lattice elements
τ_I	2 hr	Transition time scale
β	1	Self-interaction parameter
$\tilde{\gamma}$	.1	Strength of θ_{eb} coupling
$\tilde{\alpha}$	30 days	Strength of convergence coupling
R	320 km	Interaction radius

Table 1. Parameters and constants for the stochastic CIN model with non-local convergence coupling. The horizontal rules separate the basic physical scales (top), deterministic parameters, stochastic parameters from KMK03, and newly introduced non-local convergence coupling parameters (bottom). Many of these parameters are given with units, but non-dimensional forms can be obtained using the basic scales.

This is obtained by noting that the limit of the coarse-grained Hamiltonian given in (10) is

$$\lim_{q\to\infty} V(\sigma_k) = 2\beta\sigma_k + h_{ext}.$$

In a more complex model, such as Frenkel *et al.* (2012), the DMFLEs can be used as a stand-alone parameterisation which exhibits highly chaotic behaviour. However, here we only use the DMFLEs to perform the linear theory analysis of the next section. The framework also allows for interactions between different coarse-grid cells (Katsoulakis *et al.* 2003b), but using non-local convergence coupling is a simpler and better physically-motivated alternative. The next section is dedicated to developing an external potential, h_{ext}, that couples the birth-death process for σ_k to the large-scale wind convergence.

2.2. *Non-local convergence coupling*

In KMK03, the external potential, h_{ext}, which promotes the formation of convection, only depends on the boundary layer equivalent potential temperature, θ_{eb}. Specifically, $h_{ext} = -\tilde{\gamma}\theta_{eb}$, which implies that high values of θ_{eb} increase C_d, which in turns promotes the formation of convective sites. At first glance, this physical hypothesis meshes well with the boundary layer quasi-equilibrium idea (Emanuel *et al.* 1994). However, in this formulation, both CAPE and h_{ext} depend strongly on θ_{eb}. This means that CAPE and CIN are tightly coupled in this model, and that the resultant cloud fractions are closely related to convective heating rates. Therefore, this formulation fails to separate processes which increase heating per cloud from those that increase the overall number of clouds.

A simple way to eliminate this restrictively tight coupling is to allow h_{ext} to depend on some variable other than θ_{eb}. In this case, we will introduce dependence on a functional of the convergence-field. This approach is motivated by the observations (Mapes *et al.* 2006; Davies *et al.* 2013; Peters *et al.* 2013) and classic moisture convergence based parameterisations (Kuo 1974; Tiedtke 1989).

In particular, the external potential is the sum of two contributions from the large-scale variables, and is given by

$$h_{ext} = h_{\theta_{eb}} + h_w. \tag{12}$$

The first contribution, $h_{eb} = -\tilde{\gamma}\theta_{eb}$, is identical to the thermodynamic coupling of KMK03 (as stated above). The second part of the external potential, h_w is a functional of the large-scale convergence field. The intuitive idea is that positive wind convergence should promote convection by increasing the CIN death rate, which tends to decrease the overall CIN fraction.

Because the *local* wind convergence is typically evaluated as the difference of the neighbouring grid cells, it implicitly depends on the resolution of the scheme. To avoid this resolution dependent behaviour, and to allow for seamless scaling between various coarse-grid resolutions, h_w is coupled to a large-scale averaged convergence field. In particular, h_w at a given location x is assumed to be proportional to the divergence field averaged around x. Therefore, the functional form is given by

$$\begin{aligned} h_w(x) &= \tilde{\alpha}\frac{1}{2R}\int_{-R}^{R} u_x(x+x',t)dx' \\ &= \tilde{\alpha}\frac{u(x+R)-u(x-R)}{2R}, \end{aligned}$$

where the proportionality constant $\tilde{\alpha}$ is key parameter which describes the strength of the convergence coupling; the interaction radius, R, is the radius of the averaging domain. Because the unit of velocity convergence is inverse time, the parameter $\tilde{\alpha}$ can be interpreted as a time scale. The external potential can be rewritten using the shift operator, $T^R u = u(x+R)$, so that

$$h_w = \frac{\tilde{\alpha}}{2R}(T^R - T^{-R})u. \tag{13}$$

A similar averaging approach is used to allow for resolution independence in the stochastic scheme of (Plant and Craig 2008). This averaging procedure provides for a non-local coupling between coarse-grid cells, and it is necessary to the avoid the deleterious effects of wave-CISK such as grid-scale noise. This will be shown in subsequent sections.

Since we are interested in varying the model resolution in this study, some care is required to translate the continuous formation in (13) to discrete numerical context. In particular, the interaction radius must be an integer multiple of the grid size so that $R = r\Delta x$ where $r \in \mathbb{N}$. If this is true, then the interaction radius will be consistent for simulations with different numerical resolutions.

To illustrate the effect of this large-scale averaged non-local convergence coupling, the following three special cases of convergence coupling will be explored:

1. *No convergence coupling*: setting $\tilde{\alpha} = 0$ recovers the KMK03 scheme, which does not have any convergence coupling.
2. *Local convergence coupling*: taking the limit $R \to 0$ gives $h_w = \tilde{\alpha}u_x$.
3. *Non-local convergence coupling*: set $\tilde{\alpha}, R > 0$ with typical parameter values of $\tilde{\alpha} = 30$ days, and $R = 320$ km unless stated otherwise.

In the next section, linear analysis of these three cases is performed. All calculations are performed using the default parameters contained in Table 1 unless otherwise stated.

3. Linear Analysis

Linearised analysis is typically performed on a set of deterministic equations, although the notion can be extended to stochastic processes (Steinbrecher and Garbet 2012). For the present purposes, it suffices to perform the analysis on the DMFLE equations described above, which are given by dynamical core equations (1)–(4) coupled to the mean-field limit equation for the CIN fraction (11). Here, we take a continuous limit of the CIN fraction field so that the set of coarse-grid CIN fractions, $\{\sigma_k(t)\}_{0\leq k<n}$ becomes a continuous field $\sigma(x,t)$. This is trivially accomplished since (11) is just an ODE for the local CIN fraction. As mentioned before, the goal here is to study the linear effect of convergence coupling unambiguously, and WISHE is disabled in this analysis by setting the constant $C_\theta = 0$.

We linearise these equations about a radiative convective equilibrium state (RCE) and numerically investigate the resulting dispersion relation. In particular, we study the differences between no, local, and non-local convergence coupling. Finally, the effect of varying the interaction radius, R, and convergence coupling strength, $\tilde{\alpha}$, is analysed.

3.1. *Radiative convective equilibrium and linearisation*

For the purposes here, RCE is defined as a spatially homogeneous steady-state solution to the large-scale DMFLEs. In particular, we assume that the prognostic variables can be written as the sum of a constant equilibrium value and a small perturbation so that $u = \bar{u} + u'$, $\theta = \bar{\theta} + \theta'$, $\theta_{em} = \overline{\theta}_{em} + \theta'_{em}$, $\theta_{eb} = \overline{\theta}_{eb} + \theta'_{eb}$, and $\sigma = \bar{\sigma} + \sigma'$. We assume the velocity field vanishes at RCE, so that $u = u'$. In particular, we note that $\overline{u} = u_x = 0$, so that the convergence field vanishes at RCE. Throughout the paper, $\overline{X}$ is value of variable X at RCE.

Introducing the above expansions into the model equations yields at lowest order an algebraic set of equations for $\overline{\theta}$, $\overline{\theta}_{eb}$, $\overline{\theta}_{em}$, and $\overline{\sigma}$ which is given by

$$\overline{Q}_c = Q_R^0 + \frac{1}{\tau_R}\overline{\theta} \tag{14}$$

$$\frac{1}{h_b}\overline{D}(\overline{\theta}_{eb} - \overline{\theta}_{em}) = \tau_e(\theta^\star_{eb} - \overline{\theta}_{eb}) \tag{15}$$

$$\frac{1}{H}\overline{D}(\overline{\theta}_{eb} - \overline{\theta}_{em}) = Q_R^0 + \frac{1}{\tau_R}\overline{\theta} \tag{16}$$

$$\frac{1}{\tau_q}(1-\overline{\sigma}) = \frac{1}{\tau_q}\overline{\sigma}\exp(-2\beta\overline{\sigma} + \tilde{\gamma}\overline{\theta}_{eb}). \tag{17}$$

Here, the RCE diagnostic quantities $\overline{D}$, $\overline{E}$, and $\overline{Q_c}$ are obtained by substituting the RCE values of the prognostic variables into the closures described in Section 2. Of the above, (14) is obtained from the temperature equation and is a straightforward statement of equilibrium between convection and radiation. The equations above are nonlinear and are solved for $\overline{\theta}$, $\overline{\theta}_{eb}$, $\overline{\theta}_{em}$ and $\overline{\sigma}$. In practice, this is done using the `fsolve` nonlinear solver available in the `scipy` package for the `python` programming language. The parameter regime studied in this paper, which are stated in Table 1, has an unique RCE.

Linearising (1)–(4) about the RCE conditions above is done in a straightforward fashion, and very similar calculations are performed in MS01. The main difficulty lies in linearising the nonlinear diagnostic quantities Q_c and $D(\theta_{eb} - \theta_{em})$. The perturbation vertical mass flux per cloud is given by

$$w'_c = \frac{R_c}{2\overline{w_c}}(\theta'_{eb} - \gamma\theta'),$$

so that that the overall convective heating is determined by the product rule,

$$Q'_c = -\sigma_c^+\sigma'\overline{w_c} + \sigma_c^+(1-\overline{\sigma})w'_c. \tag{18}$$

At RCE, $\overline{Q_c} > 0$ so for an infinitesimal perturbation, we can assume that $Q_c + u'_x > 0$. Therefore, the downdraught mass flux is given by

$$\frac{D}{h_m} = (Q_c + u_x)^+ + \frac{1-\mu}{\mu}Q_c = \frac{Q_c}{\mu} + u'_x.$$

In particular, this shows that $\overline{Q_c} = \overline{D}$ at RCE. The perturbation downdraughts are then given by

$$\frac{D'}{h_m} = Q_c' + \mu u_x'. \tag{19}$$

The corresponding exchange of boundary layer and tropospheric equivalent potential temperature is then given by the product rule, $D^\epsilon = (D(\theta_{eb} - \theta_{em}))' = D'(\overline{\theta}_{eb} - \overline{\theta}_{em}) + \overline{D}(\theta'_{eb} - \theta'_{em})$. Finally, the evaporation term is linear and does not require special treatment because we ignore the WISHE effect by setting $C_\theta = 0$. Using these quantities, the overall linearised versions of dynamical core equations (1)–(4) can be written as

$$\frac{\partial u'}{\partial t} - \frac{\partial \theta'}{\partial x} = -\frac{1}{\tau_D} u' \tag{20}$$

$$\frac{\partial \theta'}{\partial t} - \frac{\partial u'}{\partial x} = Q_c' - \frac{1}{\tau_R}\theta' \tag{21}$$

$$h_b \frac{\partial \theta'_{eb}}{\partial t} = -D^\epsilon - \frac{\theta'_{eb}}{\tau_e} \tag{22}$$

$$H \frac{\partial \theta'_{em}}{\partial t} = D^\epsilon - \frac{H}{\tau_R}\theta' \tag{23}$$

It remains to linearise the DFMLE cloud fraction equation (11). This is accomplished using the expression

$$\sigma e^{-V} = (\overline{\sigma} + \sigma')e^{-\overline{V}-V'} = e^{-\overline{V}}\left(\bar{\sigma} + \sigma' - \bar{\sigma}V'\right),$$

which is accurate to first order. The stochastic potential V is given in (10). Finally, the linearised form of the DFMLE cloud fraction equation is given by

$$\tau_q \frac{\partial \sigma'}{\partial t} = -\sigma' - \sigma' e^{-\overline{V}} + \overline{\sigma} e^{-\overline{V}} V' \tag{24}$$

where $\bar{V} = \beta\overline{\sigma} - \tilde{\gamma}\overline{\theta}_{eb}$, and $V' = \beta\sigma' - \tilde{\gamma}\theta'_{eb} + h'_w$.

3.2. *Plane-wave solutions*

Let $\mathbf{U} = (u', \theta', \theta'_{eb}, \theta'_{em}, \sigma')^T$, and assume that $\mathbf{U} = \hat{\mathbf{U}} e^{i\{kx - \omega(k)t\} + d(k)t}$ where the phase $\omega(k)$ and growth rate $d(k)$ are both assumed to be real. The plane wave is then substituted into (20)–(24). This procedure is relatively straightforward, and is largely omitted from the discussion here. The main novelty here is the form of the convergence coupling potential h_w for a plane wave, which is different from an ordinary Fourier derivative.

For plane waves, the action of the shift operator, T^R, is a simple phase shift, which can be written mathematically as $T^R u' = e^{ikR}u'$. Therefore, for a plane wave, the convergence coupling potential becomes

$$h'_w = \tilde{\alpha}\frac{e^{ikR} - e^{-ikR}}{2R}u' = \tilde{\alpha} ik \cdot \mathrm{sinc}(kR) \cdot u', \tag{25}$$

where $\mathrm{sinc}(x) = \sin(x)/x$. For the case of local convergence coupling, taking the limit as $R \to 0$ gives $h'_w = \tilde{\alpha} iku' = \tilde{\alpha} u'_x$ for plane-waves.

After substituting the plane-wave solutions, the linearised system can be collected into a linear matrix equation given by

$$\frac{d\hat{\mathbf{U}}}{dt} = A(k)\hat{\mathbf{U}}. \tag{26}$$

The wave structures, growth rates, and phase speeds are found by solving for the eigenvalues and eigenvectors of $A(k)$. Specifically, matrix is diagonalised to obtain $A(k) = V(k)^{-1}\Lambda(k)V(k)$, where $V(k)$ are right eigenvectors of $A(k)$, and $\Lambda(k)$ is a diagonal matrix of the corresponding eigenvalues. From this diagonal form, it is trivial to extract the desired information. Let $\mathbf{v}_i$ be the i^{th} column of $V(k)$ and $\lambda_i = \Lambda_{ii}$ its corresponding eigenvalue. Then, $\mathbf{v}_i$, which is a right eigenvector of $A(k)$, describes the structure of a wave with a phase speed and growth rate given by $c_p = -Im\{\lambda_i\}/k$ and $d = Re\{\lambda_i\}$, respectively.

In the results below, this procedure is carried out numerically using the `numpy` linear algebra package for the `python` programming language. All the analyses are performed with a fixed transition time scale of $\tau_q = 2$ hr.

3.3. *Instability with high wavenumber cutoff by non-local convergence coupling*

The most interesting result of this linear analysis is that the non-local averaging operation in (13) stabilises high-wavenumber linear modes. In so doing, it allows for a convergence coupling that avoids the negative features of wave-CISK. This result can be seen in Figure 1, which plots linear phase speeds and growth rates for the cases with local and non-local convergence coupling as well as the case without any convergence coupling (KMK03). All cases feature two standing and two travelling branches with phase

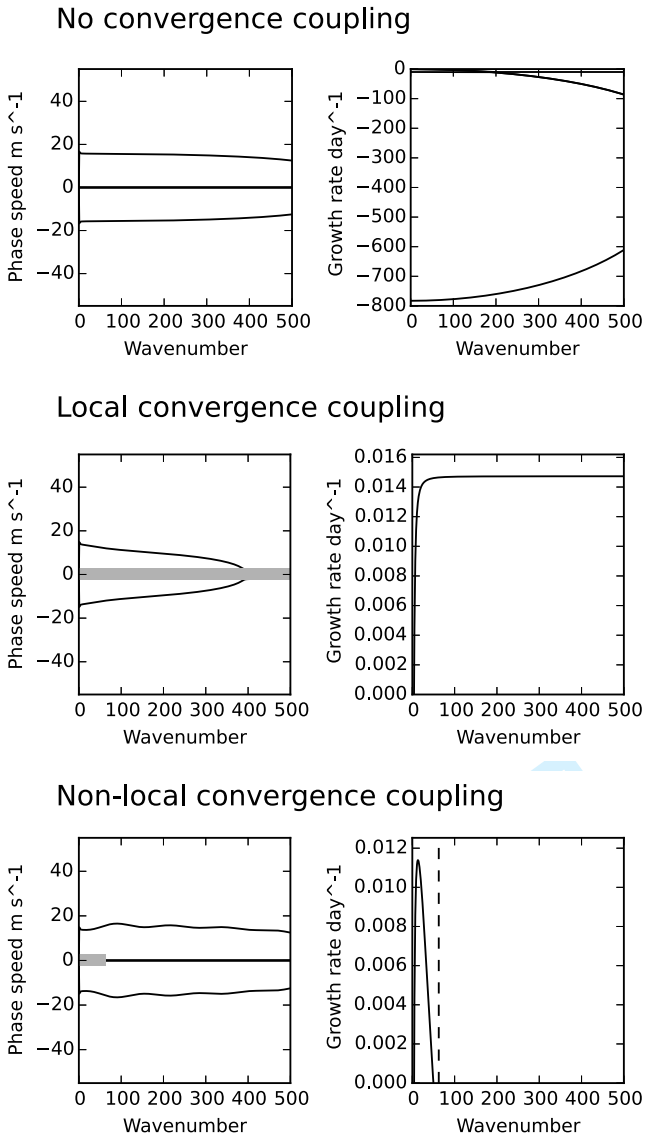

Figure 1. Generalised phase speeds (left) and growth rates (right) for the cases with no, local, and non-local convergence coupling. Note, the different scaling for the growth rate axes. For non-local convergence coupling, the wavenumber associated with the length of averaging region, $k_{crit} = (2R\,\mathrm{km})^{-1}$ is indicated (dashed). Unstable modes are highlighted in the phase speed diagrams with a thick grey line.

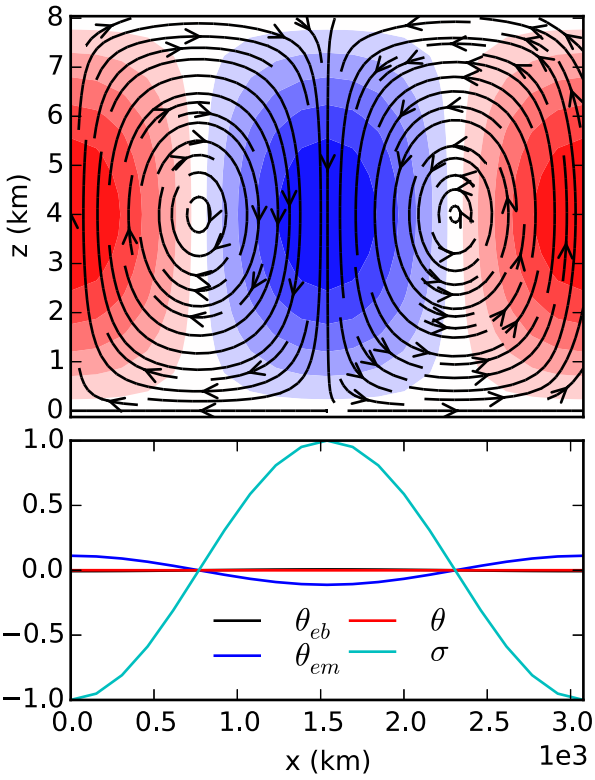

Figure 2. Structure of the unstable mode for non-local convergence coupling with wavenumber, $k = 13$, corresponding to the peak growth rate in the lower panel of Figure 1. The vertical–horizontal structure of the winds (arrows) and temperature (contours) are shown in the upper panel. Red (blue) contours indicate positive (negative) temperature anomalies. The lower panel shows the horizontal structure of the fields in non-dimensional units.

speeds less than 20 m s^{-1}, however the stability of the standing mode differs between the three cases.

Without convergence coupling, there is no instability about the RCE, but with *local* convergence coupling, there is a standing instability for all wavenumbers. Moreover, the growth rates of this instability increase with wavenumber to some asymptote. This is classic wave-CISK behaviour, and would likely manifest as grid-scale precipitation in a GCM-type simulation. On the other hand, using *non-local* convergence coupling stabilises the higher wavenumbers and restricts the instability to physically plausible scales larger than $k_{crit} = (2R\,\mathrm{km})^{-1}$, which is the wavenumber associated with the length of the averaging region.

The structure of this unstable wave for wavenumber 13, which has the maximum growth rate over all wavenumbers, is plotted in Figure 2. It is a standing wave where positive (negative) temperature anomalies occur in ascent (descent) regions. Ascending motion is most strongly associated with positive anomalies in θ_{em} and negative anomalies in the CIN fraction σ. Beyond this, it is only weakly associated with θ_{eb} and θ. This indicates that tropospheric moistening due to moisture convergence and convective triggering through mean updraughts are cooperating to produce this instability. Notably, there is actually a slight cooling of the boundary-layer below the updraught, which stands in contrast to the WISHE mechanism.

The success of the non-local convergence coupling idea in a plausible range of parameters has been demonstrated. However, it is informative to study the sensitivity to the key convergence coupling parameters: the convergence coupling strength, $\tilde{\alpha}$, and interaction radius, R. This will be done in the following sections.

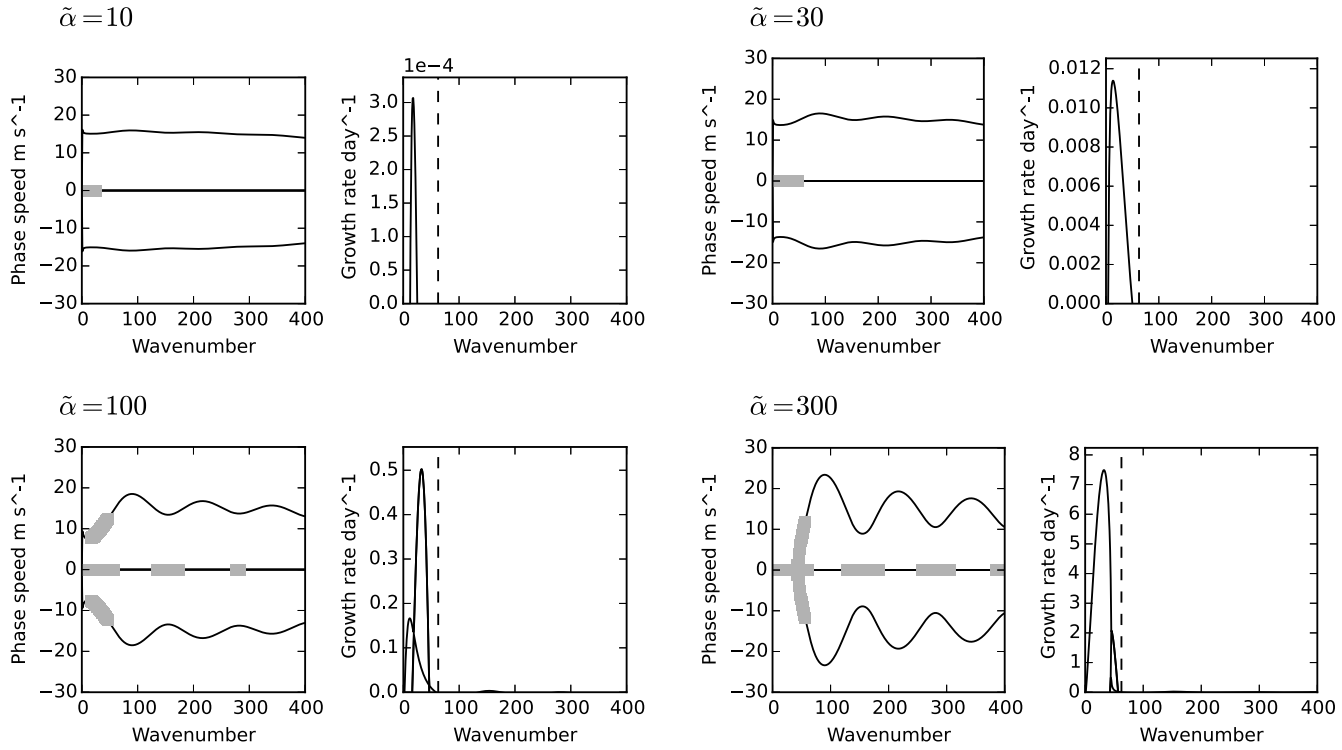

Figure 3. Linear analysis for varying $\tilde{\alpha}$ with fixed interaction radius, $R = 320$ km. As the convergence coupling strength is increased, propagating and "gap instabilities" appear. Refer to the caption of Figure 1 for a description of these diagrams.

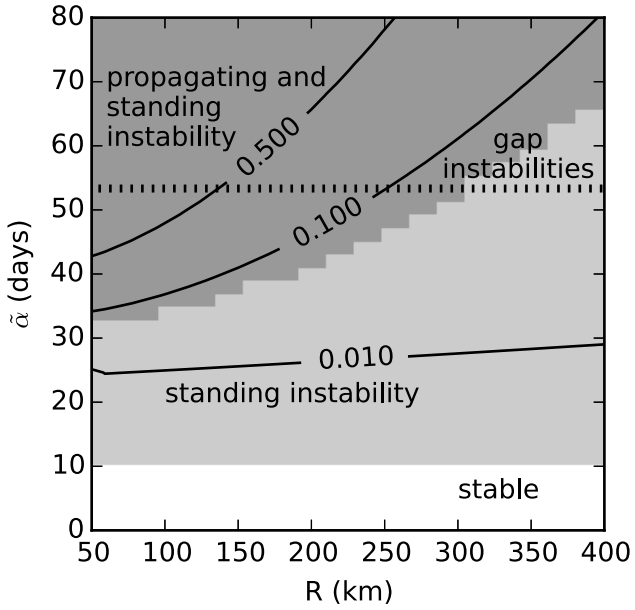

Figure 4. Stability diagram for linearised analysis. The type of instability is indicated in the regions with a solid colour. Contours indicate the maximum growth rate (day^{-1}) for all wavenumbers and solution branches. The regions of parameter space above the dashed horizontal line have "gap instabilities". These values are generated on a discretised grid of $\tilde{\alpha}$–R space.

3.4. Sensitivity to convergence coupling strength

We remind the reader that the convergence coupling strength parameter $\tilde{\alpha}$ changes the relative importance of the large-scale averaged convergence in the CIN death rate C_d. In Figure 3, we have plotted the dispersion relation diagrams for various levels of $\tilde{\alpha}$, and it is clear that increasing this parameter tends to increase the growth rates of the unstable mode.

As mentioned in Section 2.2, setting $\tilde{\alpha} = 0$ days is equivalent to using the KMK03 scheme (c.f. Figure 1), which has no explicit convergence coupling. For $10 \leq \tilde{\alpha} \leq 30$, we see that instability has a high wavenumber cutoff, and that the growth rates are increased with $\tilde{\alpha} = 30$. However, for $\tilde{\alpha} = 100, 300$ days, some new effects occur. First, scale-selective bands of instability appear above this high wavenumber cutoff. These appear as bands of positive growth rates, that occur at regular intervals in wavenumber space associated with the convergence coupling radius R; we will, hereafter, call this behaviour "gap instability". However, for all $\tilde{\alpha}$, the primary large-scale unstable band is constrained below k_{crit}, and the amplitude of the subsequent bands decrease rapidly with the wavenumber. In addition, a propagating instability with much larger growth rates than the standing instability appears for larger $\tilde{\alpha}$. This propagating instability band is bounded by k_{crit} for all $\tilde{\alpha}$. For a more complete picture, the diagram in Figure 4 shows the regions in $\tilde{\alpha} - R$ space, corresponding to standing, propagating, and "gap" instability. Finally, the phase-speeds in stable propagating bands

are increasingly effected for large values of the convergence coupling strength.

The wave number bands for frequencies higher than k_{crit} correspond to the sinc(kR) factor in the plane-wave formulation of h_w (c.f. equation 25), and could be ameliorated by using a spatial averaging operation which does not have an oscillatory response in wavenumber space. A Gaussian-weighted averaging in space is one such candidate filter. Even so, gap instabilities are not present for our best-case parameter values, and have very small growth rates compared to the large scale instability. The $\tilde{\alpha} = 100, 300$ results are only presented here as illustrative examples.

In summary, it is clear convergence coupling alters both the growth rates of the unstable waves and the phase-speeds of both stable and unstable propagating waves. In the next section, we demonstrate that the interaction radius, R, controls the permissible scales of instability.

3.5. *Sensitivity to radius of interaction*

Here, the interaction radius R is varied for a large value of convergence coupling strength, $\tilde{\alpha} = 60$ days. With this value, the linear solutions show unstable stationary and propagating modes, as well as bands of gap instability. This value of $\tilde{\alpha}$ is chosen for illustrative value rather than physical plausibility.

The linear analysis diagrams for this experiment is shown in Figure 5. As R is increased, the magnitude of the growth rates is decreased, which occurs because R approaches the decorrelation scale of the underlying wind field. Finally in all cases, it is clear that $k_{crit} = (2R)^{-1}$ is a high wavenumber cutoff for the primary branches of positive growth rates, and that R controls the locations of the higher gap instability bands. Therefore, for lower values of $\tilde{\alpha}$ without the instability bands (not shown), k_{crit} is a true high wavenumber cutoff as seen in Figures 1 and 3.

4. Idealised Walker-cell simulations

The linearised analysis of the past section points to a new scale-selective instability, and in this section, we explore the consequence of this in set of nonlinear stochastic simulations. Because classic CISK theory points to convergence coupling as an interaction mechanism between large-scale and convective flows, it is important to test these ideas in context of simulations which feature a large scale background circulation. Unlike the linearised analysis above, WISHE is allowed in these simulations for the purpose of generating waves in the absence of convergence coupling; this corresponds to setting $C_\theta > 0$ in (5). Therefore, the focus here is on investigating the interaction of non-local convergence coupling and WISHE in a model which replicates aspects of conventional QE-based parameterisations such as Arakawa and Schubert (1974); Betts and Miller (1986); Zhang and McFarlane (1995).

A large-scale Walker cell is forced here by imposing a non-uniform SST background pattern which mimics the Indian Ocean/western Pacific warm-pool. The simulations are performed in a single ring of latitude about the equator and do not include any meridional dependence. For the present context, this is accomplished by letting the sea surface saturation equivalent potential temperature take the form

$$\theta^*_{eb}(x) = 5 \cos\left(\frac{4\pi x}{40000}\right) + 10K, \tag{27}$$

within the central 20,000 km interval of the 40,000 km domain, and $\theta^*_{eb} = 5$ K elsewhere. A similar setup has been used to as dynamical test-bed in KMK03, for the stochastic multicloud model (Frenkel *et al.* 2012, 2013), and in a cloud resolving model (Slawinska *et al.* 2014, 2015). Especially in the latter two, this computationally inexpensive setup generates very interesting time series with rich convectively coupled waves and intraseasonal variability.

The numerical method used is an operator-splitting strategy where the conservative terms are discretised and solved by a non-oscillatory central scheme while the remaining convective forcing terms are handled by a second-order Runge Kutta scheme (Khouider and Majda 2005a,b). The stochastic component of the scheme is evolved using an approximation to Gillespie's exact algorithm (Gillespie 1975), which is accurate for the small time steps used here. In particular, at most one birth/death occurs per time step in each in coarse-grid cell with probabilities given by $C_a \cdot \Delta t$ and $C_d \cdot \Delta t$. See KMK03 for more details.

To replicate a typical resolution of a coarse-resolution GCM, the domain is divided into $n = 250$ grid points, unless otherwise stated, which corresponds to a grid spacing of $\Delta x = 160$ km. A

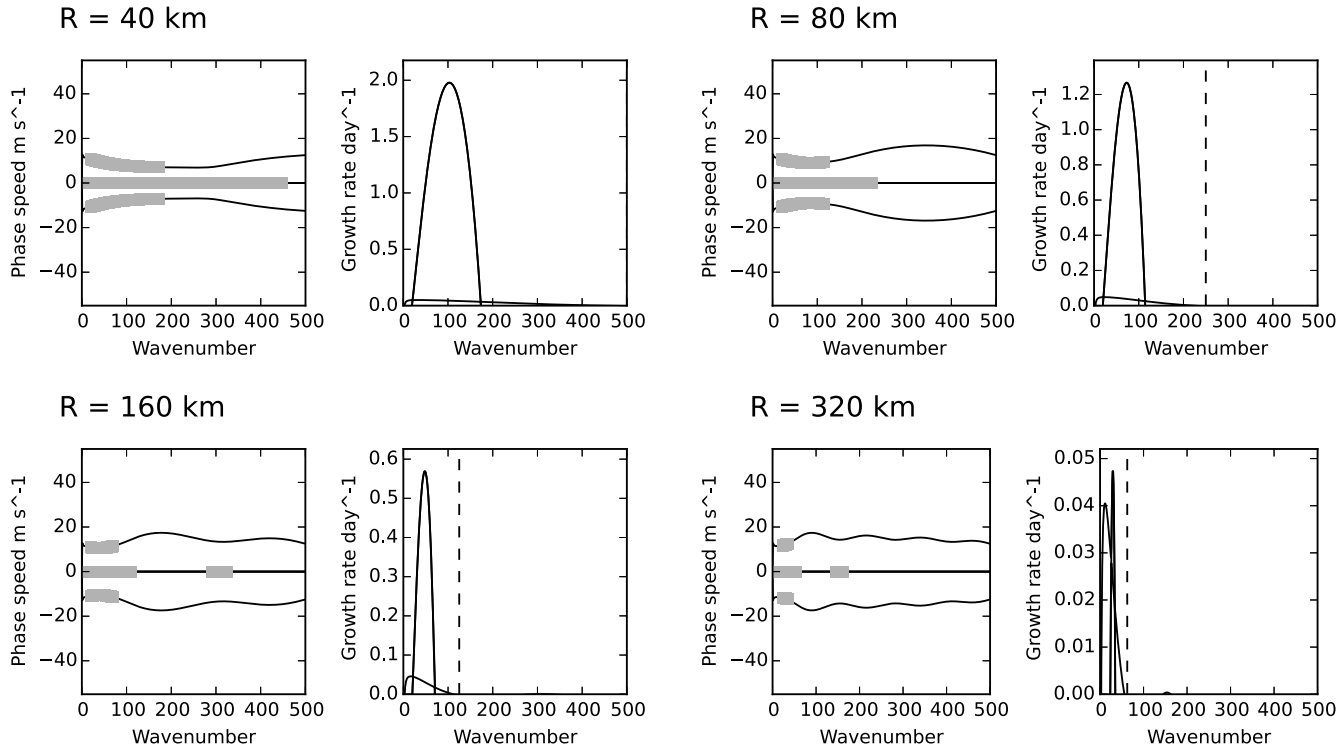

Figure 5. Same as Figure 3 but for varying interaction radius R with fixed convergence coupling strength $\tilde{\alpha} = 60$ days. For all values of R, the reference wavenumber $k_{crit} = (2R \text{ km})^{-1}$ (dashed) controls the scales of the standing, propagating, and gap instabilities.

time step of $\Delta t = 5$ minutes is used for this resolution. The other main numerical parameter, which did not factor into the linearised analysis above, is the the number of convective elements per coarse grid cell. This is fixed at $q = 12$ in all but last subsection. The transition timescale is fixed at $\tau_I = 2$ hr. To remind the reader, the stochastic dynamics approach the DFMLE for large q, but $q = 12$ is a small number of lattice elements. Stochastic fluctuation, then, plays an important role in these simulations, which are far from the linear deterministic equations studied in Section 3. The following results highlight how instability due to non-local convergence coupling manifests in a nonlinear stochastic setting. In all the simulations below, time series of 1000 days are generated, and the first 300 days are excluded from analysis.

4.1. *Effect of convergence coupling in nonlinear simulations*

Following the linearised analysis in Section 3.4, we now explore the effect of varying the convergence coupling strength parameter $\tilde{\alpha}$. The interaction radius parameter is fixed here at $R = 320$ km, which for intermediate values of $\tilde{\alpha}$ only allows synoptic scale linear instabilities with wavelengths greater than 640 km. The strength parameter is varied from $\tilde{\alpha} = 0$, which corresponds to the case without convergence coupling (e.g. KMK03), to $\tilde{\alpha} = 300$ days. The climatological velocity field, u, is shown in Figure 6, and space-time diagrams of precipitation for the final 200 days of the simulations are available in Figure 7.

Overall, the time-averaged circulation is quite similar for all values of $\tilde{\alpha}$, with a magnitude change of $\sim 1 \text{m s}^{-1}$ for larger values of $\tilde{\alpha}$. On the other hand, the convergence coupling drastically alters the variability outside of the warm-pool region between 15,000 km and 25,000 km. By examining, the Hovmoller diagrams in Figure 3, it is clear that this increased variability is associated with the propagation of convectively coupled waves (CCWs) in the dry regions of domain.

The basic KMK03 case, $\tilde{\alpha} = 0$, shows a peak of precipitation in the center of the domain–where the SSTs are highest. The CCWs are generated in the warm-pool region and propagate into the dry region, rapidly decaying as they do so. Apart from these waves, the precipitation field is quite noisy, does not feature much coherent activity, and lacks low-frequency content.

The effect that convergence coupling has on the intrinsic variability of the system is best seen in the case where the convergence coupling strength parameter $\tilde{\alpha}$ is associated with an intraseasonal to seasonal time scale, $\tilde{\alpha} = 10, 30$ days. In the linearised analysis, these values allowed for an instability

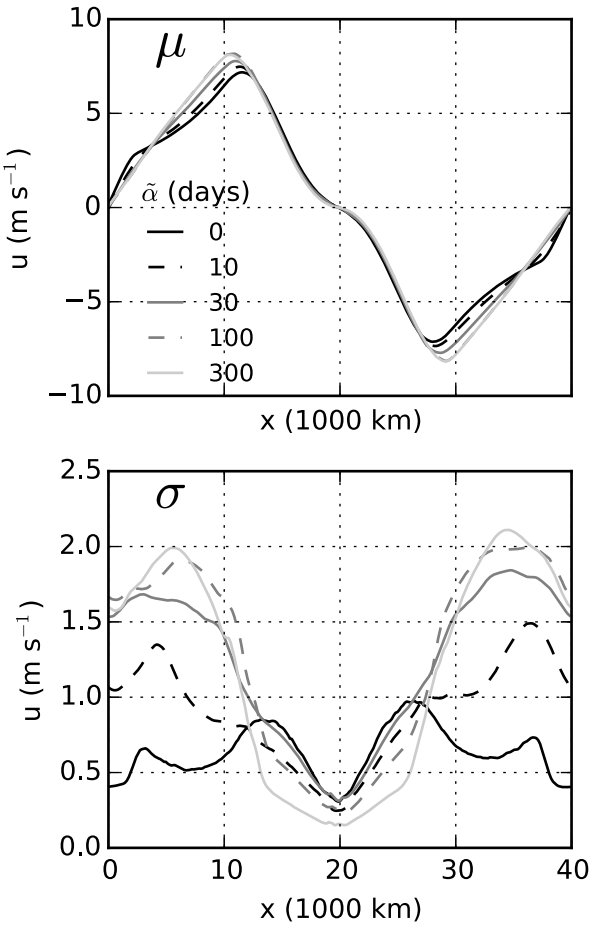

Figure 6. Temporal mean of (top) and standard deviations from the mean (bottom) of the velocity, u, for simulations with different values of $\tilde{\alpha}$ (indicated in the legend). Recall that $\tilde{\alpha} = 0$ is the reduction to the KMK03 case without convergence coupling. The non-local convergence coupling simulations using $\tilde{\alpha}$ =30 – 300 days have the strongest variability and slightly stronger mean circulations.

with a physically plausible high wavenumber cutoff. In the corresponding nonlinear simulations, batches of CCWs are generated in the warm pool at irregular intervals, and propagate much more coherently in the dry regions of the domain. The resulting variability is characterised by intermittently alternating periods of strong and weak circulation on intraseasonal and seasonal time scales. These results qualitatively resemble the CRM study of Slawinska *et al.* (2014) and results using the stochastic multicloud model (Frenkel *et al.* 2012, 2013). In particular, CCWs in the simulation with $\tilde{\alpha} = 30$ and 100 days are highly intermittent and have rich low-frequency content. From the perspective of intermittency, the results with $\tilde{\alpha} = 300$ days are less attractive because they feature more regular waves; nonetheless, these simulations still display low frequency content.

To quantitatively demonstrate the intraseasonal variability of the dynamics seen in Figure 7, normalised power spectra of the velocity time series for three representative spatial locations are shown in Figure 8. These power spectra are calculated using Welch's method with a segment length of 128 days. For the driest region of the domain, $x = 0$ km, the convergence coupled simulations show more power overall, but especially at lower frequencies. The enhanced low frequency variability of the convergence coupled simulations is most distinctly visible at $x = 10,000$ km, which marks the edge of the warm-pool—the region with the most CCW activity. In the very centre of the warm pool, $x = 20,000$ km, the overall power is less in the convergence coupled simulations than in the KMK03 case (e.g. $\tilde{\alpha} = 0$), but there is strong shift towards lower frequency.

These results are not particular sensitive to the interaction radius parameter, R, (not shown) and show remarkable robustness over several orders of magnitude of the parameter $\tilde{\alpha}$. Of these, the most interesting case is $\tilde{\alpha} = 30$ days, a regime which has standing, but not propagating, linear instabilities according to Figure 4. In the following section, the sensitivity of these results to numerical resolution is studied.

4.2. *Effect of varying resolution*

One of the key reasons for introducing stochasticity in convective parameterisations is to allow a seamless scalability from coarse to fine resolutions. Indeed, the non-local convergence coupling formulated in Section 2.2 is specifically designed with this in mind, and uses a spatial averaging operation along the lines of (Plant and Craig 2008). Here, we test the scalability of the scheme, by performing simulations with our most interesting case (non-local convergence coupling with $\tilde{\alpha} = 30$ days and $R = 320$ km) on 40, 80 and 160 km grids. In addition to the resolution, the number of convective elements per coarse grid cell, q, is also varied in an effort to deduce a proper scaling—a similar analysis is done in Frenkel *et al.* (2012).

A first attempt to preserve the statistical structure of the variability is achieved by keeping the number of CIN sites per unit length constant. This amounts to varying the the number of elements, q, linearly with respect to the grid-size, Δx. This crude scaling law could likely be improved, but that is not the focus here. As mentioned in Section 2.2, the interaction radius $R = 320$ km, is a integer multiple of each these grid sizes, which allows for a seamless translation between the continuous and discrete

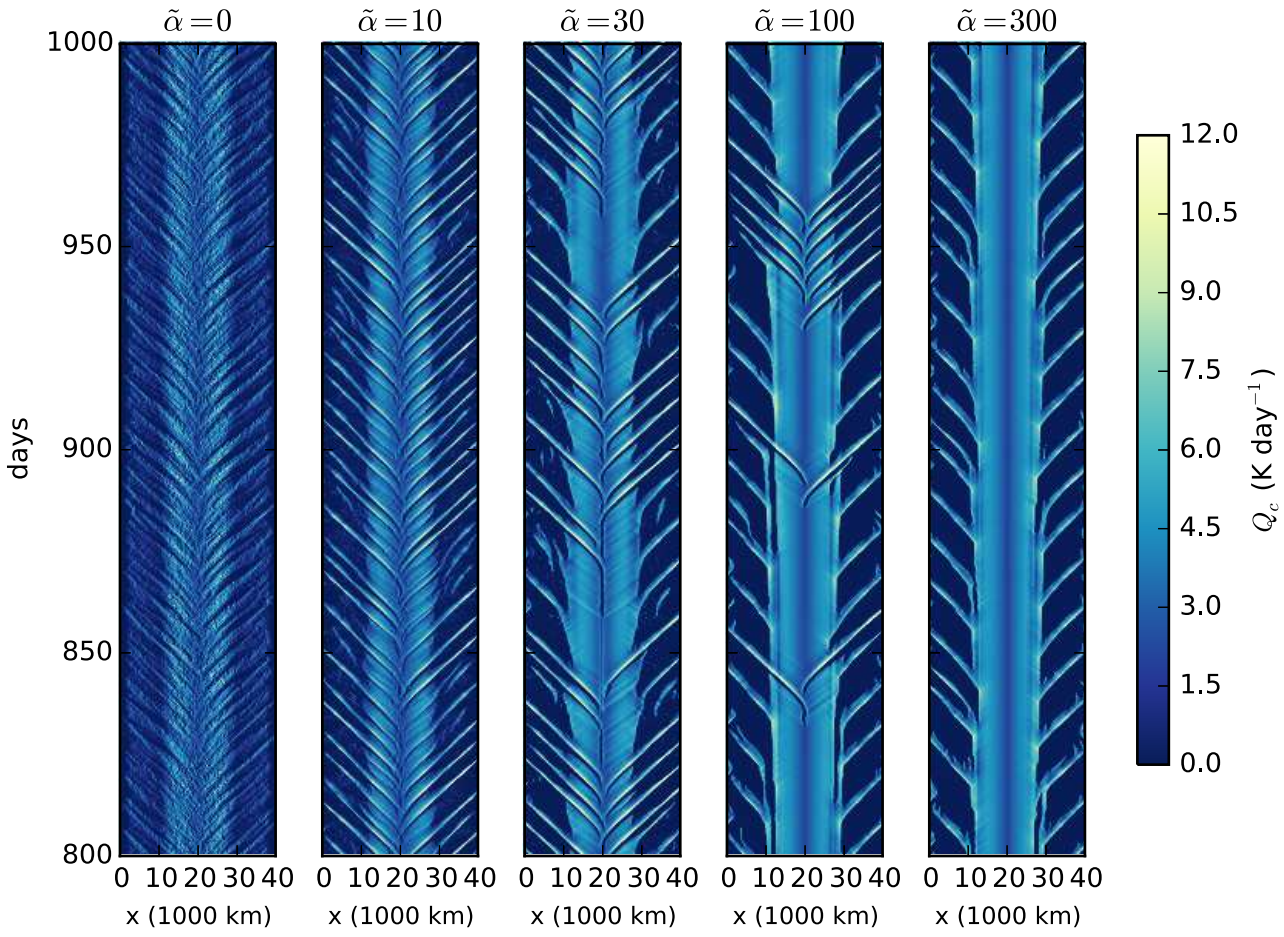

Figure 7. Hovmoller diagrams of precipitation for simulations with different values of $\tilde{\alpha}$. The case where the convergence coupling parameter, $\tilde{\alpha}$, is set to 30 days exhibits low frequency variability. The effect we observed is robust over over the several order of magnitude range of the coupling constant.

formulations of the non-local convergence coupling. For example, $\Delta x = 40$ km implies that the discrete radius of interaction is $r = R/\Delta x = 8$ grid cells.

The climatological wind fields for these simulations, which are plotted in Figure 9, shows that all simulations have nearly identical mean states throughout the domain, but differing variability structure. For the most part, the higher resolution simulations have more variability inside than outside outside the warm-pool. However, certain simulations do show good agreement throughout the domain. For example, compare the 160 km and 80 km simulations with $q = 48$ and $q = 24$, respectively.

Corresponding to these climatological results, space-time diagrams of precipitation are available in Figure 10. Overall, the low-frequency behaviour due to convergence coupling is robust for several different resolutions and values of q. For example, each panel in left column of Figure 10 shows a well defined low-frequency oscillation as was discussed in Section 3.4. That said, the scaling with resolution is imprecise. For smaller number of lattice elements and finer resolutions, this low-frequency behaviour is also visible; however, the simulations in the lower-right panels, display a different zoology of CCWs. These CCWs are generated frequently at regular time intervals in the centre of the domain.

The impreciseness of the scaling law is possibly due to the relatively low number of lattice elements used here, or because the stochastic coupling uses a local rather than large-scale value of θ_{eb}. We expect that as the number of lattice elements, q, is increased — and the system approaches its mean field limit — a more precise scaling law can be deduced. For example, the scaling analysis in Frenkel *et al.* (2012), which used simulations with about 900 lattice elements, suggested that the proper scaling is not necessarily linear. However, using such a high number of lattice elements in this simple model leads to phenomenologically less interesting results without attractive intermittency. Because these details are not specific to the non-local convergence coupling introduced here, we do not consider them in further detail.

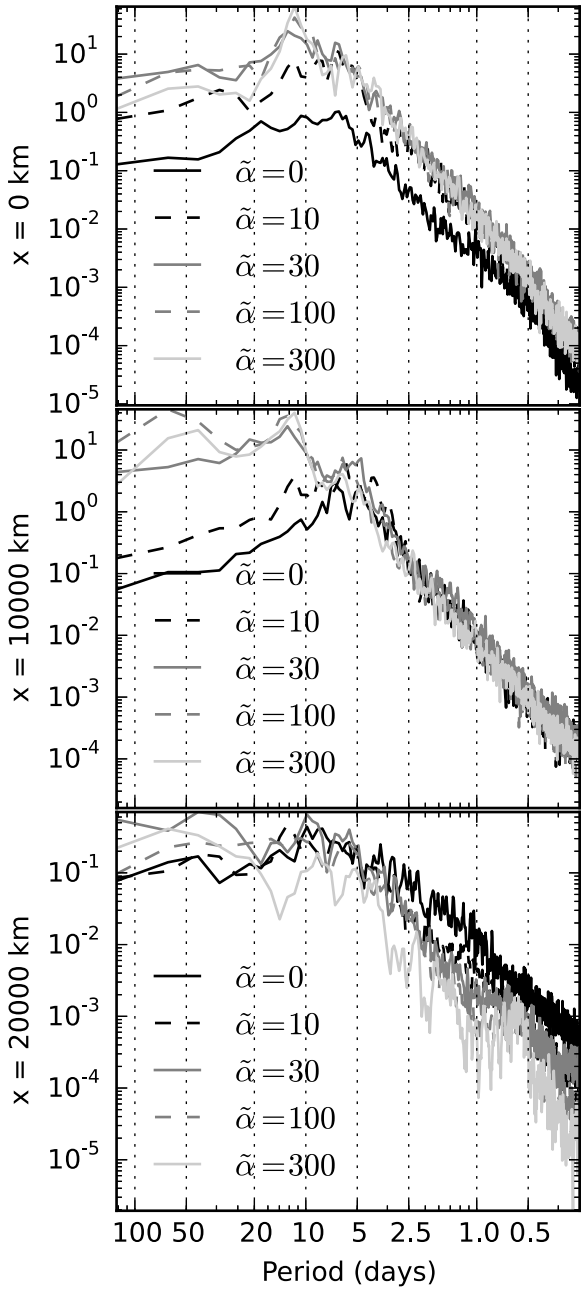

Figure 8. Power spectrum of the velocity for three different spatial locations: the driest region (0 km), the edge of the warm pool (10,000 km), and the centre of the warm pool (20,000 km). As the value of convergence coupling strength parameter is increased we observe progressive shift towards longer time scales. The effect is most distinct in the region of active wave propagation around x =10,000 km.

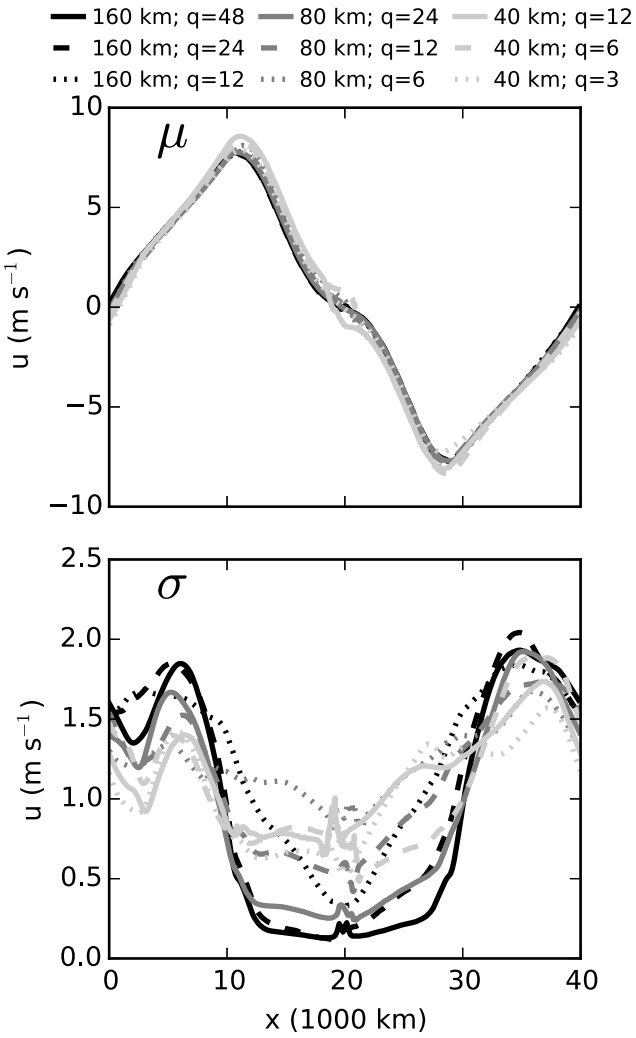

Figure 9. Temporal mean (top) and standard deviations (bottom) of the velocity field, u, for simulations associated with various number of convective elements for: 160 km (black), 80 km (dark grey) and 40 km (light grey) grid.

5. Conclusions

In this paper, we have introduced a mechanism for non-local convergence coupling into a simplified stochastic model that mimics aspects of current GCM parameterisations. Because the model consists of only one baroclinic mode it cannot represent the effect of congestus heating, stratiform heating, nor the observed vertical tilt of convectively coupled waves in the tropics. This model was chosen as a simple test-bed to study the dynamical ramifications of *non-local* convergence coupling and to address the criticisms of *local* convergence coupling raised in Emanuel *et al.* (1994).

Linearised analysis of the deterministic mean-field limit equations unambiguously shows that using non-local convergence coupling ameliorates some of the problems of wave-CISK. Specifically, averaging the convergence field over some radius of interaction before coupling it to the death rate of CIN sites imposes a high wavenumber cutoff for the instability in realistic parameter regimes. Moreover, the high wavenumber cutoff is set by the size of the averaging region. On the other hand, coupling the CIN death rate to the *local* convergence field leads to classic CISK-type behaviour with small-scale instability.

The nature of the instability depends on the strength of the convergence coupling, and it is possible to obtain both stationary and propagating instabilities for different parameter regimes. However, the propagating instability is not present for more

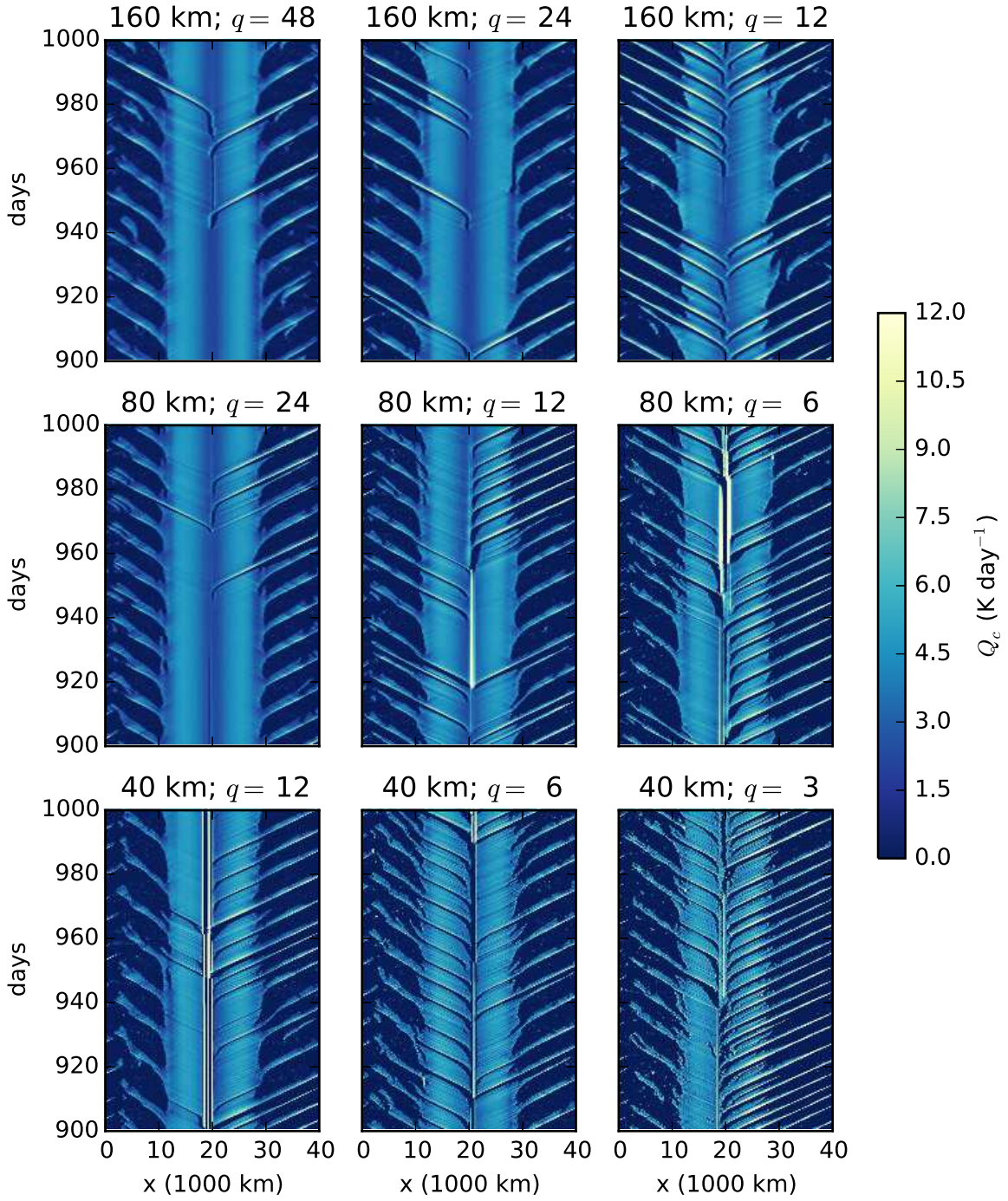

Figure 10. Hovmoller diagrams of precipitation anomalies for the various grid size/number of convective elements combinations shown in Figure 9. The grid-size, Δx decreases from top to bottom, and the number of lattice elements, q, decreases from left to right. In each column, the simulations obey a linear scaling between Δx and q. The linear scaling best preserves the qualitative structure for the case with the largest number of elements (leftmost column).

physically plausible parameter choices. The unstable stationary wave has a structure indicating a strong feedback between mid-tropospheric humidity and grid-averaged updraughts due to increased cloud fractions.

The linearised analysis also showed that strong convergence coupling leads to scale-selective bands of "gap" instability for high wavenumbers with diminishing growth rates. This numerical artefact is due to the oscillatory wavenumber-response of the simple spatial averaging procedure used here, and would likely be eliminated using a Gaussian-weighted averaging method. This suggests that such a weighted averaging operation should be used whenever large-scale averaged fields are used in a stochastic convective parameterisation. However, it is questionable how important this effect is in the full nonlinear simulations.

From the perspective of the nonlinear and stochastic idealised Walker-cell simulations, non-local convergence coupling gives rise to an attractive zoology of convectively coupled waves. These waves are associated with low-frequency variability of

the Walker circulation on intraseasonal time scales, and are extremely intermittent in nature. This low-frequency behaviour is qualitatively similar to that seen in a similar set of cloud resolving simulations (Slawinska *et al.* 2014). On the other hand, the simulations with WISHE alone lack any low-frequency content, and have much more noisy precipitation fields. This contrasts with the conventional notion that convergence coupling leads to grid-scale noise, which may be true for the classical Kuo-type moisture budget closures, but is not the case for the *non-local* convergence coupling introduced here.

Finally, these stochastic closures show decent scalability across different resolutions, which is an important consideration as GCM grid-sizes begin to resolve the mesoscale. However, the model used here is intended to replicate the behaviour of coarse-resolution GCMs and does not account for important aspects of mesoscale organisation such as stratiform rain. Sophisticated mesoscale-aware parameterisations such as the multicloud models are able to produce intraseasonal variability in idealised Walker cell simulations (Frenkel *et al.* 2013), but not without additional overhead. Therefore, it appears that the non-locality of the convergence coupling introduced here acts as a surrogate for unresolved horizontal and vertical structures. In so doing, it is able to mimic aspects of more realistic models.

Acknowledgements

The research of A. J. M. is partially supported by the Office of Naval Research MURI award grant ONR-MURI N-000-1412-10912. Y. F. is a postdoctoral fellow supported through the above MURI award, and N.D.B. is supported as a graduate student on the MURI award.

References

Ajayamohan RS, Khouider B, Majda AJ. 2013. Realistic initiation and dynamics of the madden-julian oscillation in a coarse resolution aquaplanet gcm. *Geophys. Res. Lett.* **40**(23): 6252–6257, doi:10.1002/2013gl058187.

Ajayamohan RS, Khouider B, Majda AJ. 2014. Simulation of monsoon intraseasonal oscillations in a coarse-resolution aquaplanet gcm. *Geophys. Res. Lett.* **41**(15): 5662–5669, doi:10.1002/2014gl060662.

Arakawa A. 2004. The cumulus parameterization problem: Past, present, and future. *J. Climate* **17**(13): 2493–2525, doi:10.1175/1520-0442(2004)017<2493:ratcpp>2.0.co;2.

Arakawa A, Schubert WH. 1974. Interaction of a cumulus cloud ensemble with the large-scale environment, part i. *J. Atmos. Sci.* **31**(3): 674–701, doi:10.1175/1520-0469(1974)031<0674:ioacce>2.0.co;2.

Betts AK, Miller MJ. 1986. A new convective adjustment scheme. part ii: Single column tests using gate wave, bomex, atex and arctic air-mass data sets. *Quarterly Journal of the Royal Meteorological Society* **112**(473): 693–709, doi:10.1002/qj.49711247308.

Buizza R, Milleer M, Palmer TN. 1999. Stochastic representation of model uncertainties in the ecmwf ensemble prediction system. *Quarterly Journal of the Royal Meteorological Society* **125**(560): 2887–2908, doi:10.1002/qj.49712556006.

Charney JG, Eliassen A. 1964. On the growth of the hurricane depression. *Journal of the Atmospheric Sciences* **21**(1): 68–75, doi:10.1175/1520-0469(1964)021<0068:otgoth>2.0.co;2.

Crommelin D, Vanden-Eijnden E. 2008. Subgrid-scale parameterization with conditional markov chains. *J. Atmos. Sci.* **65**(8): 2661–2675, doi:10.1175/2008jas2566.1.

Crueger T, Stevens B, Brokopf R. 2013. The madden–julian oscillation in echam6 and the introduction of an objective mjo metric. *J. Climate* **26**(10): 3241–3257, doi:10.1175/jcli-d-12-00413.1.

Davies L, Jakob C, May P, Kumar VV, Xie S. 2013. Relationships between the large-scale atmosphere and the small-scale convective state for darwin, australia. *Journal of Geophysical Research: Atmospheres* **118**(20): 11,534–11,545, doi:10.1002/jgrd.50645.

Del Genio AD, Chen Y, Kim D, Yao MS. 2012. The mjo transition from shallow to deep convection in cloudsat /calipso data and giss gcm simulations. *J. Climate* **25**(11): 3755–3770, doi:10.1175/jcli-d-11-00384.1.

Deng Q, Khouider B, Majda AJ. 2015. The mjo in a coarse-resolution gcm with a stochastic multicloud parameterization. *J. Atmos. Sci.* **72**(1): 55–74, doi:10.1175/jas-d-14-0120.1.

Emanuel KA, David Neelin J, Bretherton CS. 1994. On large-scale circulations in convecting atmospheres. *Quarterly Journal of the Royal Meteorological Society* **120**(519): 1111–1143, doi:10.1002/qj.49712051902.

Frenkel Y, Majda AJ, Khouider B. 2012. Using the stochastic multicloud model to improve tropical convective parameterization: A paradigm example. *J. Atmos. Sci.* **69**(3): 1080–1105, doi:10.1175/jas-d-11-0148.1.

Frenkel Y, Majda AJ, Khouider B. 2013. Stochastic and deterministic multicloud parameterizations for tropical convection. *Climate Dynamics* **41**(5-6): 1527–1551, doi:10.1007/s00382-013-1678-z.

Gillespie DT. 1975. An exact method for numerically simulating the stochastic coalescence process in a cloud. *J. Atmos. Sci.* **32**(10): 1977–1989, doi:10.1175/1520-0469(1975)032<1977:aemfns>2.0.co;2.

Grabowski WW, Yano JI, Moncrieff MW. 2000. Cloud resolving modeling of tropical circulations driven by large-scale sst gradients. *J. Atmos. Sci.* **57**(13): 2022–2040, doi:10.1175/1520-0469(2000)057<2022:crmotc>2.0.co;2.

Holloway CE, Neelin JD. 2009. Moisture vertical structure, column water vapor, and tropical deep convection. *J. Atmos. Sci.* **66**(6): 1665–1683, doi: 10.1175/2008jas2806.1.

Kain JS, Fritsch JM. 1990. A one-dimensional entraining/detraining plume model and its application in convective parameterization. *J. Atmos. Sci.* **47**(23): 2784–2802, doi:10.1175/1520-0469(1990)047<2784:aodepm>2.0.co;2.

Katsoulakis MA, Majda AJ, Vlachos DG. 2003a. Coarse-grained stochastic processes and monte carlo simulations in lattice systems. *Journal of Computational Physics* **186**(1): 250–278, doi:10.1016/s0021-9991(03)00051-2.

Katsoulakis MA, Majda AJ, Vlachos DG. 2003b. Coarse-grained stochastic processes for microscopic lattice systems. *Proceedings of the National Academy of Sciences* **100**(3): 782–787, doi:10.1073/pnas.242741499.

Khouider B, Biello J, Majda AJ. 2010. A stochastic multicloud model for tropical convection. *Commun. Math. Sci.* **8**(1): 187–216.

Khouider B, Majda AJ. 2005a. A non-oscillatory balanced scheme for an idealized tropical climate model. *Theoretical and Computational Fluid Dynamics* **19**(5): 331–354, doi:10.1007/s00162-005-0170-8.

Khouider B, Majda AJ. 2005b. A non-oscillatory balanced scheme for an idealized tropical climate model. *Theoretical and Computational Fluid Dynamics* **19**(5): 355–375, doi:10.1007/s00162-005-0171-7.

Khouider B, Majda AJ, Katsoulakis MA. 2003. Coarse-grained stochastic models for tropical convection and climate. *Proceedings of the National Academy of Sciences* **100**(21): 11 941–11 946, doi: 10.1073/pnas.1634951100.

Khouider B, St-Cyr A, Majda AJ, Tribbia J. 2011. The mjo and convectively coupled waves in a coarse-resolution gcm with a simple multicloud parameterization. *J. Atmos. Sci.* **68**(2): 240–264, doi: 10.1175/2010jas3443.1.

Kiladis GN, Wheeler MC, Haertel PT, Straub KH, Roundy PE. 2009. Convectively coupled equatorial waves. *Reviews of Geophysics* **47**(2), doi: 10.1029/2008rg000266.

Kuo HL. 1974. Further studies of the parameterization of the influence of cumulus convection on large-scale flow. *J. Atmos. Sci.* **31**(5): 1232–1240, doi:10.1175/1520-0469(1974)031<1232:fsotpo>2.0.co;2.

Lau WKM, Waliser DE. 2012. *Intraseasonal variability in the atmosphere-ocean climate system*. Springer Berlin Heidelberg, doi:10.1007/978-3-642-13914-7.

Lin JWB. 2003. Toward stochastic deep convective parameterization in general circulation models. *Geophys. Res. Lett.* **30**(4), doi:10.1029/2002gl016203.

Lin JWB, Neelin JD. 2000. Influence of a stochastic moist convective parameterization on tropical climate variability. *Geophys. Res. Lett.* **27**(22): 3691–3694, doi:10.1029/2000gl011964.

Lindzen RS. 1974. Wave-cisk in the tropics. *J. Atmos. Sci.* **31**(1): 156–179, doi:10.1175/1520-0469(1974)031<0156:wcitt>2.0.co;2.

Majda AJ, Franzke C, Khouider B. 2008. An applied mathematics perspective on stochastic modelling for climate. *Philosophical Transactions of the Royal Society A: Mathematical, Physical and Engineering Sciences* **366**(1875): 2427–2453, doi:10.1098/rsta.2008.0012.

Majda AJ, Khouider B. 2002. Stochastic and mesoscopic models for tropical convection. *Proceedings of the National Academy of Sciences* **99**(3): 1123–1128, doi:10.1073/pnas.032663199.

Majda AJ, Shefter MG. 2001a. Models for stratiform instability and convectively coupled waves. *J. Atmos. Sci.* **58**(12): 1567–1584, doi: 10.1175/1520-0469(2001)058<1567:mfsiac>2.0.co;2.

Majda AJ, Shefter MG. 2001b. Waves and instabilities for model tropical convective parameterizations. *J. Atmos. Sci.* **58**(8): 896–914, doi: 10.1175/1520-0469(2001)058<0896:waifmt>2.0.co;2.

Majda AJ, Stechmann SN. 2008. Stochastic models for convective momentum transport. *Proceedings of the National Academy of Sciences* **105**(46): 17 614–17 619, doi:10.1073/pnas.0806838105.

MANABE S, SMAGORINSKY J, STRICKLER RF. 1965. Simulated climatology of a general circulation model with a hydrologic cycle 1. *Monthly Weather Review* **93**(12): 769–798, doi:10.1175/1520-0493(1965)093<0769:scoagc>2.3.co;2.

Mapes B, Tulich S, Lin J, Zuidema P. 2006. The mesoscale convection life cycle: Building block or prototype for large-scale tropical waves? *Dynamics of Atmospheres and Oceans* **42**(1-4): 3–29, doi: 10.1016/j.dynatmoce.2006.03.003.

Mapes BE. 2000. Convective inhibition, subgrid-scale triggering energy, and stratiform instability in a toy tropical wave model. *J. Atmos. Sci.* **57**(10): 1515–1535, doi:10.1175/1520-0469(2000)057<1515:cisste>2.0.co;2.

Moncrieff MW, Klinker E. 1997. Organized convective systems in the tropical western pacific as a process in general circulation models: A toga coare case-study. *Quarterly Journal of the Royal Meteorological Society* **123**(540): 805–827, doi:10.1002/qj.49712354002.

Nakazawa T. 1988. Tropical super clusters within intraseasonal variations over the western pacific. *Journal of the Meteorological Society of Japan. Ser. II* **66**(6): 823–839.

Palmer TN. 2001. A nonlinear dynamical perspective on model error: A proposal for non-local stochastic-dynamic parametrization in weather and climate prediction models. *Quarterly Journal of the Royal Meteorological Society* **127**(572): 279–304, doi:10.1002/qj.49712757202.

Peters K, Jakob C, Davies L, Khouider B, Majda AJ. 2013. Stochastic behavior of tropical convection in observations and a multicloud model. *J. Atmos. Sci.* **70**(11): 3556–3575, doi:10.1175/jas-d-13-031.1.

Plant RS, Craig GC. 2008. A stochastic parameterization for deep convection based on equilibrium statistics. *J. Atmos. Sci.* **65**(1): 87–105, doi: 10.1175/2007jas2263.1.

Raymond DJ, Herman MJ. 2011. Convective quasi-equilibrium reconsidered. *J. Adv. Model. Earth Syst.* **3**(8), doi:10.1029/2011ms000079.

Scinocca JF, McFarlane NA. 2004. The variability of modeled tropical precipitation. *J. Atmos. Sci.* **61**(16): 1993–2015, doi:10.1175/1520-0469(2004)061<1993:tvomtp>2.0.co;2.

Slawinska J, Pauluis O, Majda AJ, Grabowski WW. 2014. Multiscale interactions in an idealized walker circulation: Mean circulation and intraseasonal variability. *J. Atmos. Sci.* **71**(3): 953–971, doi:10.1175/jas-d-13-018.1.

Slawinska J, Pauluis O, Majda AJ, Grabowski WW. 2015. Multiscale interactions in an idealized walker cell: Simulations with sparse space–time superparameterization. *Monthly Weather Review* **143**(2): 563–580, doi:10.1175/mwr-d-14-00082.1.

Slingo JM, Sperber KR, Boyle JS, Ceron JP, Dix M, Dugas B, Ebisuzaki W, Fyfe J, Gregory D, Gueremy JF, et al. 1996. Intraseasonal oscillations in 15 atmospheric general circulation models: results from an amip diagnostic subproject. *Climate Dynamics* **12**(5): 325–357, doi:10.1007/bf00231106.

Steinbrecher G, Garbet X. 2012. Linear stochastic stability analysis of nonlinear systems. Parametric destabilization of the wave propagation. *arXiv:1212.1365 [math-ph]* URL `http://arxiv.org/abs/1212.1365`. ArXiv: 1212.1365.

Suhas E, Zhang GJ. 2014. Evaluation of trigger functions for convective parameterization schemes using observations. *J. Climate* **27**(20): 7647–7666, doi:10.1175/jcli-d-13-00718.1.

Tiedtke M. 1989. A comprehensive mass flux scheme for cumulus parameterization in large-scale models. *Monthly Weather Review* **117**(8): 1779–1800, doi:10.1175/1520-0493(1989)117<1779:acmfsf>2.0.co;2.

Zhang C. 2005. Madden-julian oscillation. *Reviews of Geophysics* **43**(2), doi:10.1029/2004rg000158.

Zhang G, McFarlane NA. 1995. Sensitivity of climate simulations to the parameterization of cumulus convection in the canadian climate centre general circulation model. *Atmosphere-Ocean* **33**(3): 407–446, doi:10.1080/07055900.1995.9649539.